Applied Physics, Material Sciences, and Engineering Journal
ISSN 3065-1425
Volume 13 Issue 2
April-June 2025
Impact Factor: 8.13
Enquiry: contact@continentalpub.online
Published by Continental Publication | https://cspjournals.org/index.php/apmsej

MECHANISMS OF TEMPERATURE ELEVATION AND WAVEFRONT BROADENING FROM NANOSCALE HE BUBBLES IN SHOCKED COPPER

Meilin Qiang Zhang
Laboratory of Computational Physics, Institute of Applied Physics and Computational Mathematics, Beijing 100094, China

Abstract: *This study employs molecular dynamics simulations to examine the dynamic behavior of nanoscale helium bubbles with distinct morphologies in a copper matrix subjected to shock wave loading. Three ellipsoidal configurations are analyzed: prolate (HB-I), oblate (HB-II), and spherical (HB-III), each with axes aligned along the shock propagation direction. The simulations reveal that HB-I, with its major axis aligned to the shock direction, generates the highest temperature rise and thermal energy accumulation due to its pronounced interfacial curvature. As shock waves interact with the helium bubbles, refraction at the bubble-matrix interface leads to wavefront broadening, which is also most significant in the HB-I case. Furthermore, surface integrity analyses of near-surface bubbles indicate that HB-I is the most prone to interface breakage under varying impact velocities, exhibiting the lowest threshold particle velocity required for damage initiation. These findings highlight the critical role of bubble morphology in influencing thermal and mechanical responses of irradiated metals under extreme dynamic conditions.*

Keywords: *Helium bubbles, shock loading, molecular dynamics, wavefront broadening*

Introduction

Helium (He) bubbles are a typical type of defect formed in metals when exposed to radiation environments.[1] The influence of helium bubbles on the dynamic behavior of metals is a critical concern in inertial confinement fusion (ICF) and aerospace engineering. These helium bubbles in metals are typically nano-scaled, with the number densities of 10^{17}–10^{18} and high internal pressure in the order of gigapascals.[2,3] The presence of helium bubbles can lead to hardening, embrittlement, and irradiation swelling of metals,[4–8] all of which significantly affect the dynamic mechanical properties.

Previous experimental studies have demonstrated that helium bubbles affect the dynamic mechanical properties of metals, such as yield strength and spall strength.[9–12] Wang et al.[9] reported significant hardening of copper at helium implantation doses up to 2×10^{17} ions/cm^2. Fan et al.[10] conducted an in situ micropillar compression test inside a scanning electron microscope (SEM) and observed that the irradiated copper (Cu) exhibited an ultrahigh yield strength of ~1.6 GPa. Katoh et al.[4] discovered that helium implantation moderately mitigated irradiation-induced hardening at doses of 10 and 100 appm when the temperature is below 673 K. Lear et al.[12] found that both yield strength and hardness increase with

Vol. 13 No. 2 | Imp. Factor: 8.13
DOI: https://doi.org/10.5281/zenodo.15845920
helium dose from 1000 to 4000 appm, while the Richtmyer– Meshkov instability experiment revealed no significant strength changes in the same dose ranges as compared to unimplanted Cu at the strain rate of 10^8/s.

Helium bubbles have also been shown to influence the spall strength of metals.[13–16] Glam et al.[13] introduced helium into aluminum-based samples via neutron irradiation and investigated its effects on spallation using gas gun impact experiments. They found that, at 873 K, the spall strength of Al-^{10}B with helium bubbles was significantly reduced compared to that of helium-free Al-^{10}B, whereas no significant difference was observed at room temperature (298 K).[14,15] In addition to spall behavior, helium bubbles also affect the micro-jetting process of metals under shock loading. Fensin et al.[11] investigated the effect of helium implantation on ejecta production in copper using Richtmyer–Meshkov instability experiments and found that the ejecta velocity increases by 30% in copper implanted with 4000 appm helium compared to unimplanted copper.

In recent years, researchers have also conducted extensive numerical simulations and theoretical studies on the influence of helium bubbles on dynamic mechanical properties.[17–23] Kubota et al.[18] investigated the yield strength of Al containing helium bubbles by molecular dynamics (MD) simulations and found that their presence enhanced the yield strength under impact pressures ranging from 0 to 40 GPa, in agreement with experimental observations. Zhu et al.[19] performed MD simulations on bicrystal Cu containing helium bubbles under uniaxial compression and tension. Their results revealed that all the bubble-containing samples exhibited lower yield stresses and strains than the bubble-free sample, regardless of loading directions or helium bubble positions. MD simulation results also indicate that helium bubbles can reduce the spall strength of metals. Shao et al.[20] investigated the influence of helium bubbles on the spallation of Al and found that the spall strength of samples containing helium bubbles reduced by 2.6 GPa from 11.8 GPa (in a perfect sample). Jiang et al.[21] revealed a competitive relationship between the expansion of helium bubbles and the nucleation and growth of voids during spallation. They also found that the presence of grain boundaries could mitigate the reduction in spall strength caused by helium bubbles, reducing their weakening effect by approximately 50%.[22] Moreover, the presence of helium bubbles can influence the micro-jetting behavior of metals. Li et al.[24] found that near-surface helium bubbles could burst under strong shock, producing high-velocity ejecta composed of atoms and small fragments.[25,26] Flanagan et al.[27] investigated the effect of random helium distributions and morphologies on ejecta production with a flat surface, observing that helium bubbles produced 56% more ejected mass than atomic helium. Our previous work examined the effects of He bubbles on micro-jet formation on a perturbation surface, finding that the expansion of helium bubbles can accelerate the velocity of the jet head and increase the ejecta mass under both single and double shock loading.[28,29]

Spallation can occur in metals containing helium bubbles under Taylor wave loading. Previous experimental and simulation studies have indicated that the spall damage process in metals containing helium bubbles is dominated by the expansion and coalescence of helium bubbles.[14,21,30,31] Experimental micrographs reveal that helium bubbles in damaged metals can exhibit different morphologies, such as sphere and ellipsoid.[7,14] These morphological differences could affect the

Vol. 13 No. 2 | Imp. Factor: 8.13
DOI: https://doi.org/10.5281/zenodo.15845920

propagation of a double shock wave and the thermodynamic response of metals. However, research on the effect of helium bubbles with different morphologies under shock condition is still lacking.

In this work, the MD simulations have been employed to investigate the dynamic mechanical response of helium bubbles with different morphologies within a copper matrix under supported shock wave loading. The investigated morphologies consist of three types of ellipsoidal configurations with axes aligned with the shock propagation direction: prolate (HB-I, major axis aligned), oblate (HB-II, minor axis aligned), and spherical (HB-III, equal axes). The organization of this paper is as follows. In Sec. II, a detailed description of the methods and simulation is provided. The results and discussion are given in Sec. III. In Sec. III A, the microstructure evolution of a bulk helium bubble is revealed. In Sec. III B, we analyze the differences in the temperature induced by different types of helium bubbles. Then, the physical mechanisms underlying the propagation of the shock wave within the helium bubble have been discussed in Sec. III C. In Sec. III D, the differences in surface damage induced by a helium bubble with different morphologies are revealed. Finally, in Sec. IV, we draw conclusions based on the results.

II. METHODOLOGY

The molecular dynamics simulations are performed by a Large-scale Atomic/Molecular Massively Parallel Simulator (LAMMPS) code[32] with the Embedded Atom Method (EAM) potential developed by Mishin et al.[33] For Cu, previous studies have shown that this potential can accurately describe the highpressure melting curve and the equation of state.[34,35] The interatomic interactions of Cu–He and He–He are described by Lennard–Jones (LJ) potentials. The parameters a, b, ϵ, and σ for LJ potential f(r) ¼ 4εhσ_r^a σ_r^bi are, respectively, set to be 9, 6 ,
0.000745, and 3.546 Å for Cu–He interactions and 12, 6, 0.000876 , and 2.280 Å for the He–He interaction, respectively.[36] The accuracy of these interaction parameters under high-pressure shock loading has been widely proved in previous investigations.[37,38]

The simulation setup in this work is shown in Fig. 1. The facecentered cubic (FCC) lattice configuration of single crystal Cu was used to construct the supercell. The lattice constant is 3.615 Å. The supercell is oriented along x [100], y [010], and z [001] axes. The size of the supercell is 60 × 60 × 300 lattice units, resulting in a cell volume of 21.7 × 21.7 × 108.5 nm^3 with 4 320 000 atoms. One

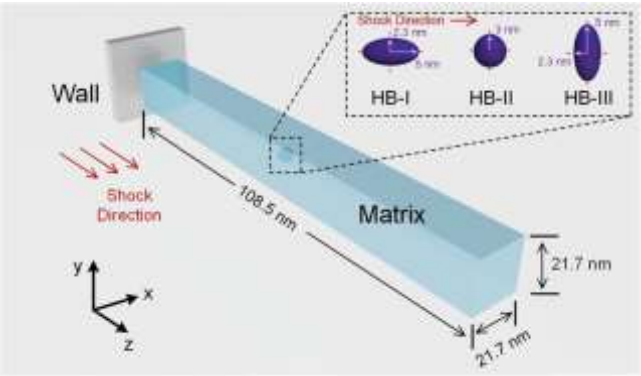

FIG. 1. Simulation setup. The Cu matrix is colored by blue, and the He bubble is colored by purple.

Vol. 13 No. 2 | Imp. Factor: 8.13
DOI: https://doi.org/10.5281/zenodo.15845920

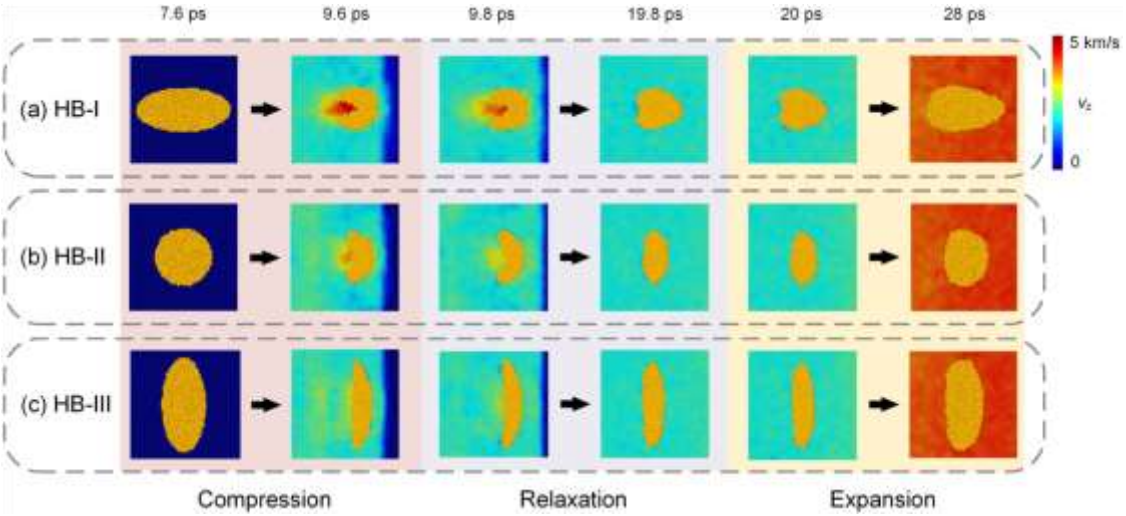

FIG. 2. Dynamic evolution of the He bubble for (a) HB-I, (b) HB-II, and (c) HB-III during shock wave loadings with u_p = 2.0 km/s. Cu atoms are colored according to velocities, while He atoms are colored in yellow for clarify. Different background colors divide the evolution process into three stages.

helium bubble is introduced into the Cu sample. The morphology of the helium bubble varies along the shock direction, including an ellipsoid with a major radius along the shock direction (marked as HB-I), a sphere (marked as HB-II), and an ellipsoid with a minor radius along the shock direction (marked as HB-III). The length of a semi-major axis of HB-I and HB-III is 5 nm, and the length of a semi-minor axis of HB-I and HB-III is 2.3 nm, as shown in Fig. 1. The radius of HB-II is 3 nm.

For the three types of He bubbles, the volume (113 nm^3), the He/vacancy ratio (1:1), and the number of helium atoms (~9600) are all the same.

First, the sample is relaxed at 300 K and zero pressure with the isothermal–isobaric (NPT) ensemble with three dimensional (3 D) periodic boundary conditions for 20 ps. Then, the shock loading process

Vol. 13 No. 2 | Imp. Factor: 8.13
DOI: https://doi.org/10.5281/zenodo.15845920
is simulated with a microcanonical (NVE) ensemble. A rigid wall is set at the lowest z position of the supercell and is driven to impact the sample at a velocity of u_p, generating a supported shock wave propagating in the z direction. In all shock simulations, a periodic boundary condition is applied only in the x and y directions, while the z direction of the sample is regarded as a free surface. The integration time step is set to 0.5 fs, and u_p varies from 1.0 to 3.5 km/s.

III. RESULTS AND DISCUSSION

A. Microstructure evolution of a He bubble during shock loadings

Figure 2 presents the microstructure evolution of the He bubble with u_p = 2.0 km/s. The moment when a shock wave begins to propagate from the left surface of the Cu matrix is set to 0 ps. It is found that the dynamic evolution process of different morphologies of the He bubble can be divided into three

FIG. 4. The probability distribution function of high-temperature particles induced by He bubbles with different morphologies at (a) u_p = 1.0 km/s, (b) u_p = 2.0 km/s, and (c) u_p = 3.5 km/s. (d) The relationship between thermal energy accumulation Q in copper induced by different types of He bubbles and the post-shock particle velocity.

stages: (I) compression, (II) relaxation, and (III) expansion.

The shock wave reaches the left interface of the He bubble at

DOI: https://doi.org/10.5281/zenodo.15845920

stage, the He bubble is compressed, and the left interface of the He bubble shrinks inward. After the HB-I is fully compressed, an internal micro-jet forms within the bubble, while the HB-II forms a weak internal micro-jet and the HB-III only experiences compres sion. After the He bubble is compressed, the shock wave reflects at the free surface, and the rarefaction wave reaches the right surface of the He bubble, leading to the formation of the relaxation stage.

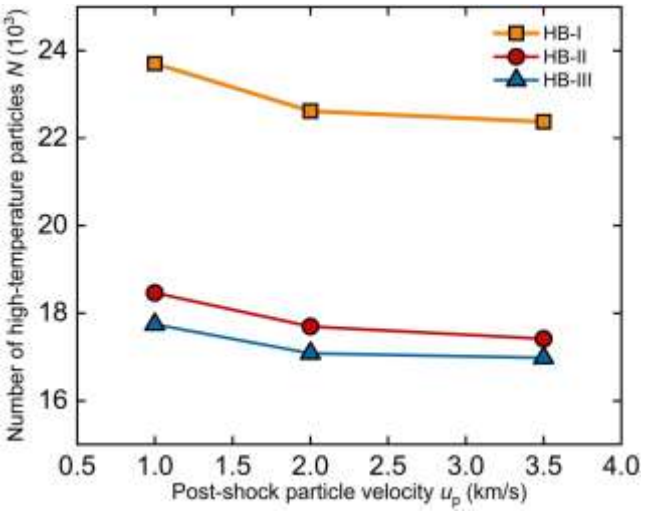

7.8 ps and passes through the He bubble within ~2 ps. During this

FIG. 3. The number of high-temperature particles (N) induced by the He bubbles under different u_p.

The internal micro-jet in HB-I disappears, while the inward shrinkage of HB-II and HB-III is recovered. Finally, the rarefaction wave sweeps over the He bubble during the expansion stage (t > 20 ps), causing the He bubble to expand.

B. The discrepancy of temperature rising with the closure of different morphologies of He bubbles

To characterize the temperature rise induced by the He bubble, the number of high-temperature particles surrounding the He bubble is counted. The statistical temperature threshold T_1 is calculated byT_1 ¼ aT_0, where T_0 is the average post-shock particle temperature and a (a > 1) is an empirical coefficient. Here, Cu atoms with temperatures higher than T_1 are counted as hightemperature particles. The post-shock particle temperature of Cu atoms follows the Maxwell–Boltzmann distribution. The empirical coefficient a is set to 1.3, which can effectively distinguish whether high-temperature particles are caused by the temperature rise effect generated by helium bubble compression and expansion or the temperature rise introduced by shock wave loading. For cases of u_p equal to 1.0, 2.0, and 3.5 km/s, the corresponding T_1 values are 845, 2951, and 9451 K, respectively. The number of hightemperature particles (N) corresponding to different u_p for the three types of He bubbles is shown in Fig. 3. It is observed that HB-I induces the most number of high-temperature particles under the same u_p.

We then compared the probability distribution of hightemperature particles at different temperatures for three types of He bubbles by calculating the probability distribution function f. The f represents the probability of particles appearing within different temperature intervals, with a statistical interval length of 100 K, as shown in Figs. 4(a)–4(c). The probability distribution of hightemperature particles with a relatively low temperature is very similar for all three types of He bubbles. However, the

Vol. 13 No. 2 | Imp. Factor: 8.13
DOI: https://doi.org/10.5281/zenodo.15845920

probability distribution of high-temperature particles in the three types of helium bubbles gradually differs as the temperature increases. At different u_p, the probability of a high-temperature particle

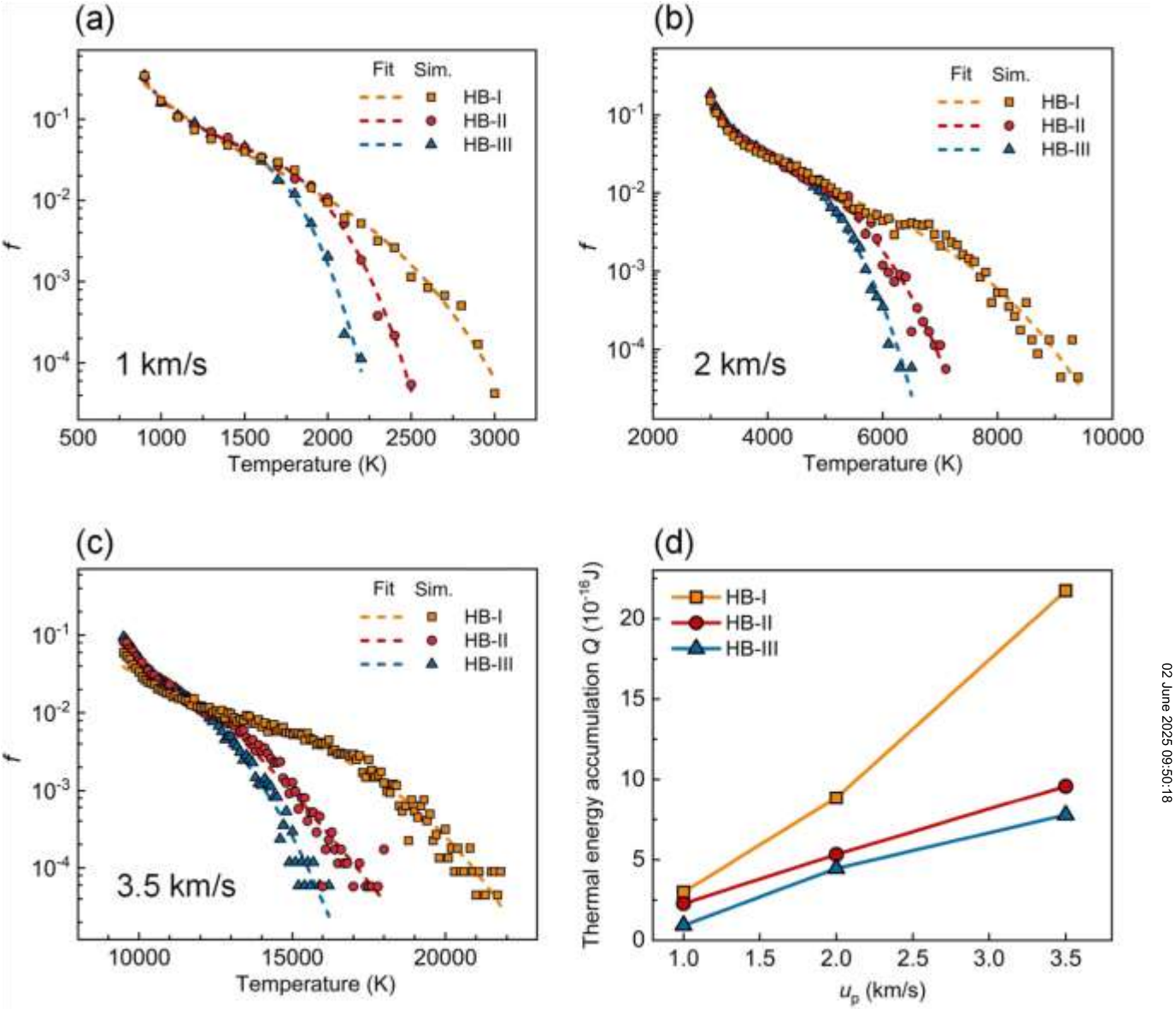

number distribution for HB-I is significantly higher than the other two types of helium bubbles. The probability distribution function can be fitted by the following equation:

$$f(T) = \exp(AT^3 + BT^2 + CT + D), \quad (1)$$

where T is the temperature and A, B, C, and D are, respectively, fitting parameters. Based on this, we calculated the thermal energy accumulation Q in the Cu matrix induced by the He bubble, which is defined by

$$Q = C_{Cu} m_{atom} N \int_{T_1}^{T_{max}} f(T)\,dT, \quad (2)$$

where C_{Cu} is the specific heat capacity of copper, m_{atom} is the mass of a single Cu atom, and N is the number of high-temperature particles. The relationship between the thermal energy accumulation Q and u_p for the three types of He bubble is shown in Fig. 4(d). The results show that $Q_I > Q_{II} > Q_{III}$ for

Vol. 13 No. 2 | Imp. Factor: 8.13
DOI: https://doi.org/10.5281/zenodo.15845920

different u_p. Furthermore, the discrepancy in thermal energy accumulation becomes more pronounced between HB-I and the others as u_p increases.

The discrepancy in the probability distribution of hightemperature particles is related to the morphologies of He bubbles. We then show the intersecting surface diagrams of different morphologies of the He bubble in Fig. 5. Different types of He bubbles have different curvatures, resulting in different energy accumulation effects relative to the direction of shock wave propagation.

To investigate the differences of curvature between helium bubbles, we regarded the left interface of the helium bubble as a type of surface disturbance and compared the equivalent $k_{eff}h_o$ values of cross sections of He bubbles. The $k_{eff}h_o$ value is calculated using the effective area formula proposed by Cherne et al.[39–41] k_{eff} is the wavenumber ($k_{eff} = 2\pi/\lambda_{eff}$, and λ_{eff} is the equivalent wavelength of a sinusoidal disturbance), and h_o is the amplitude, which equals half the distance from peak to valley for a sinusoidal disturbance. The larger the $k_{eff}h_o$, the greater the curvature of the He bubble interface. The λ_{eff} is defined by $\lambda_{eff} = A/h_o$, where A is the area of the initial surface perturbation.[39] For helium bubbles, A is

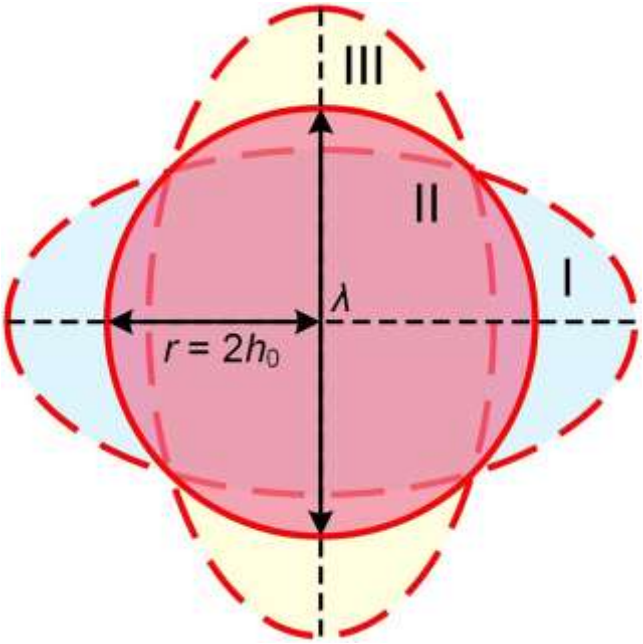

FIG. 5. The intersecting surface diagrams of He bubbles. The red solid circle represents HB-II, the blue ellipse represents HB-I, and the yellow ellipse represents HB-III.

calculated by $0.5A_{HB}$, where A_{HB} is the maximum cross-sectional area of helium bubbles along the impact direction. The surface perturbation parameters of He bubbles with different morphologies obtained according to the above definition are shown in Table I. The results show that HB-I has the largest $k_{eff}h_o$ value. Thus, the curvature of the helium bubble interface perpendicular to the shock wave front is greater than others. Therefore, the helium bubble interface will obtain a higher transversal velocity perpendicular to the shock direction, resulting in a stronger energy accumulation effect. To clarify the effects of a $k_{eff}h_o$ value, we further show the results of the interface velocities and the transverse component of different types of helium bubbles in Fig. 6.

The interface velocity for different morphologies of He bubbles is shown in Fig. 6(d). The interface velocity is determined by averaging the velocities of Cu atoms in a thin layer at the interface on the

Vol. 13 No. 2 | Imp. Factor: 8.13
DOI: https://doi.org/10.5281/zenodo.15845920

symmetry axis of the helium bubble. The interface velocity rises to its maximum value and then decreases to the value

TABLE I. The surface perturbation parameters of He bubbles with different morphologies.

	AHB (nm2)	Ahalf (nm2)	h_o (nm)	λ_{eff} (nm)	keffho
HB-I	36.51	18.25	2.50	7.30	2.15
HB-II	28.27	14.14	1.50	9.43	1.00
HB-III	36.51	18.25	1.16	15.71	0.47

Vol. 13 No. 2 | Imp. Factor: 8.13
DOI: https://doi.org/10.5281/zenodo.15845920

of u_p (2.0

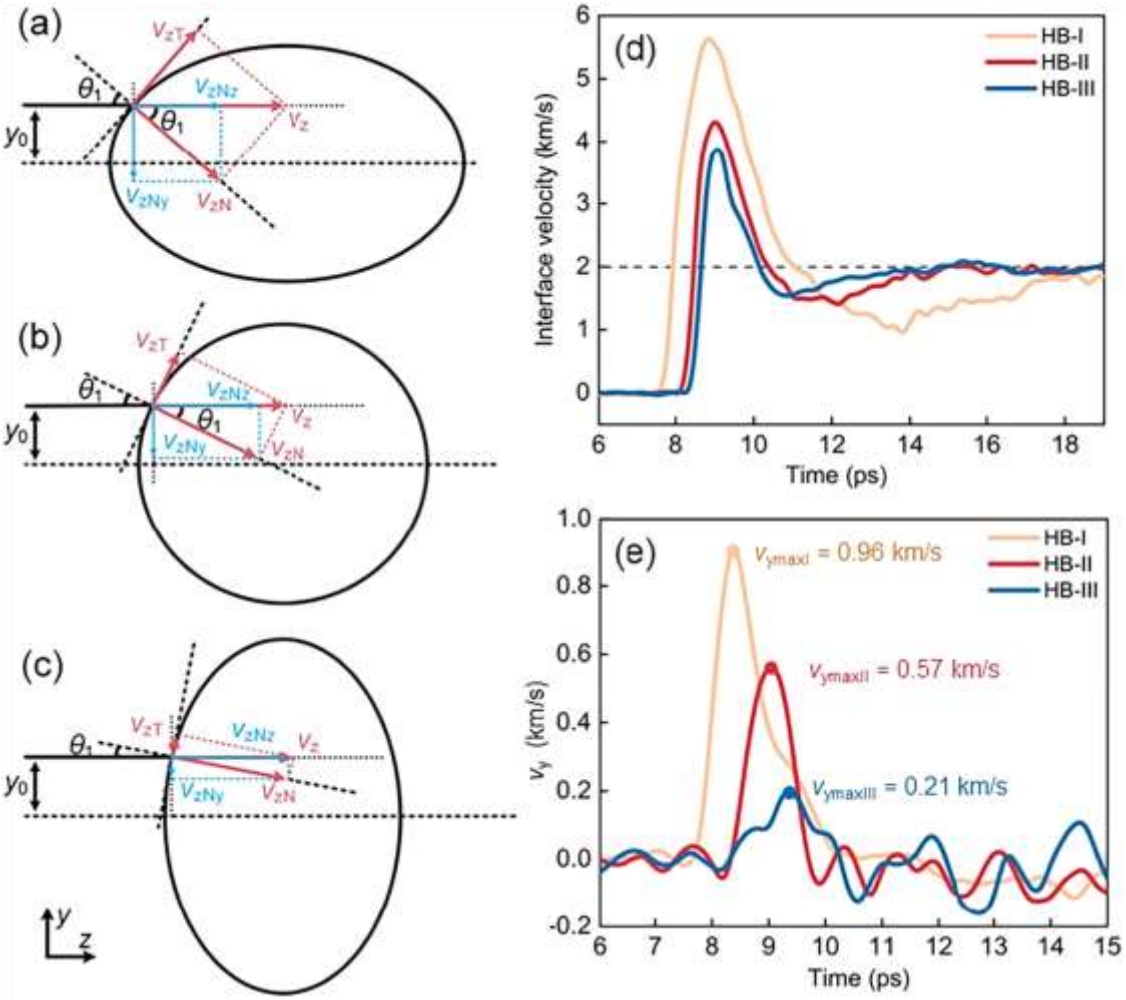

FIG. 6. The components of the longitudinal velocity (v_z) on the copper/bubble interface for (a) HB-I, (b) HB-II, and (c) HB-III. Temporal evolution of (d) v_z of the Cu matrix at the copper/bubble interface and (e) the transverse component of the velocity (v_y) of the Cu matrix velocity at the interface between copper and helium bubbles.

km/s) for all three types of He bubbles. The portion of the curve above the dashed line corresponds to the growth process of the internal micro-jet, while after that, the portion below the dashed line corresponds to the retraction of the internal micro-jet until it disappears. HB-I generates the strongest internal micro-jet, with the highest maximum interface velocity among the three types of helium bubbles. In addition, the internal micro-jet in HB-I takes the longest time to retract and completely disappear. In contrast, the internal micro-jets generated by HB-II and HB-III are less pronounced, with lower maximum interface velocities, and the internal micro-jets disappear more quickly, with the interface velocity reaching u_p earlier. Figure 6(e) provides the evolution of the transverse component of velocity (v_y) of Cu atoms located at the interface 1.5 nm from the symmetry axis of the helium bubble. The maximum of v_y for the three types of He bubbles is marked by v_{ymaxI}, v_{ymaxII}, and $v_{ymaxIII}$, respectively, as shown in Fig. 6(e). The results indicate that, as predicted based on the equivalent $k_{eff}h_o$ value, the transverse component of the velocity follows the trends of $v_{ymaxI} > v_{ymaxII} > v_{ymaxIII}$. It suggests that HB-I has the strongest energy gathering effect, and the particles on both sides of the symmetry

Vol. 13 No. 2 | Imp. Factor: 8.13
DOI: https://doi.org/10.5281/zenodo.15845920
axis of HB-I convert more kinetic energy into thermal energy during the collision process, resulting in higher thermal energy accumulation Q induced by HB-I, as shown in Fig. 4(d).

C. The mechanism of non-planar shock front formation

Previous research studies have shown that non-planar shock fronts are formed when a shock wave passes through regions of a metal containing He bubbles.[12,27,29] The broadening of the shock front could affect the surface breakage behavior of the metal.[27] We

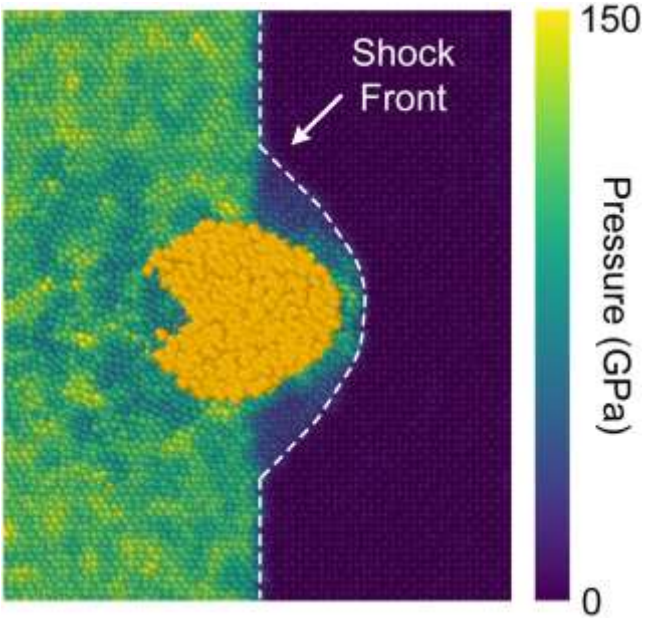

FIG. 7. The front of the shock wave after passing HB-I. The shock front is marked by the white dashed line. The He atoms are colored in orange, and the Cu atoms are colored by pressure.

tracked the process of shock front broadening as the shock wave passes through the He bubble with different morphologies. The front of the shock wave after passing HB-I is shown by the white dashed line in Fig. 7. The results show that the shock wave is scattered when it passes through the He bubble, resulting in the formation of a non-planar shock front.

We then investigated the propagation of the shock wave within the He bubble. When the shock wave obliquely shocks the Cu–He interface, its propagation direction is deflected, as shown in Fig. 8(a). Here, θ_1 is the angle between the incident shock wave and the normal to the interface, and θ_2 is the angle between the transmitted shock wave and the normal to the interface. θ_1 and θ_2 are related to the shock wave propagation speed through the relationship $\frac{\sin\theta_1}{\sin\theta_2} = \frac{D_{Cu}}{D_{He}}$, where D_{Cu} and D_{He} represent the shock wave velocities in the Cu matrix and the He bubble, respectively. We obtained D_{Cu} and D_{He} by using MD calculations. By tracking the positions of the shock front at different times, D_{Cu} and D_{He} can be obtained directly from the MD simulation result, where

$D_{Cu} = 6.8$ km/s and $D_{He} = 8.7$ km/s.

As the shock wave passes through the He bubble, it undergoes deflection at both the incident and emission points, as shown in Fig. 8(b). Since the initial incident shock wave S_1 and the incident angle θ_1 are already determined, the relationship between θ_1 and θ_2 at the incident position can be derived. This allows for the determination of the shock wave's propagation path S_2 within the He bubble and the emission position. Subsequently, θ_3 and θ_4 can be determined, ultimately leading to the determination of the emission shock wave S_3. The propagation path of the shock wave and the position of the

Vol. 13 No. 2 | Imp. Factor: 8.13
DOI: https://doi.org/10.5281/zenodo.15845920
wavefront after it passes through the He bubble are determined by this method. The result shows that the shock wave is scattered by the He bubble and cause the formation of nonplanar shock front, as shown in Fig. 8(c).

We present the shock wave front and post-wave states of copper colored by pressure and temperature to compare the theoretical analysis and simulation results of shock wave deflection when shock waves are incident on Cu–He interfaces of different types of He bubbles, as shown in Fig. 9. The results show that the

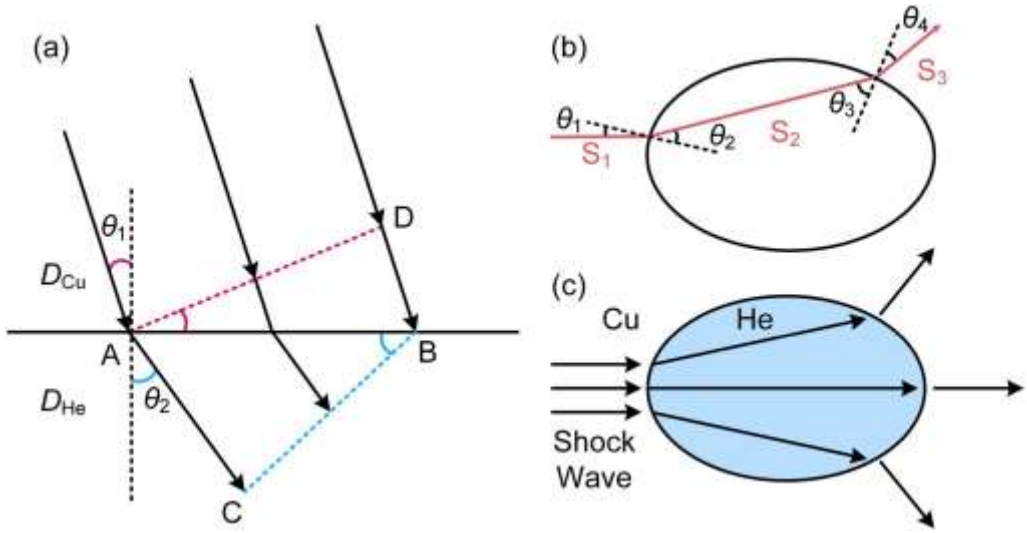

FIG. 8. Schematic illustrations of (a) the deflection of the shock wave upon oblique incidence on the Cu–He interface, (b) the two deflections of the shock wave as it propagates through a He bubble, and (c) the scattering of a shock wave by an He bubble.

Vol. 13 No. 2 | Imp. Factor: 8.13
DOI: https://doi.org/10.5281/zenodo.15845920

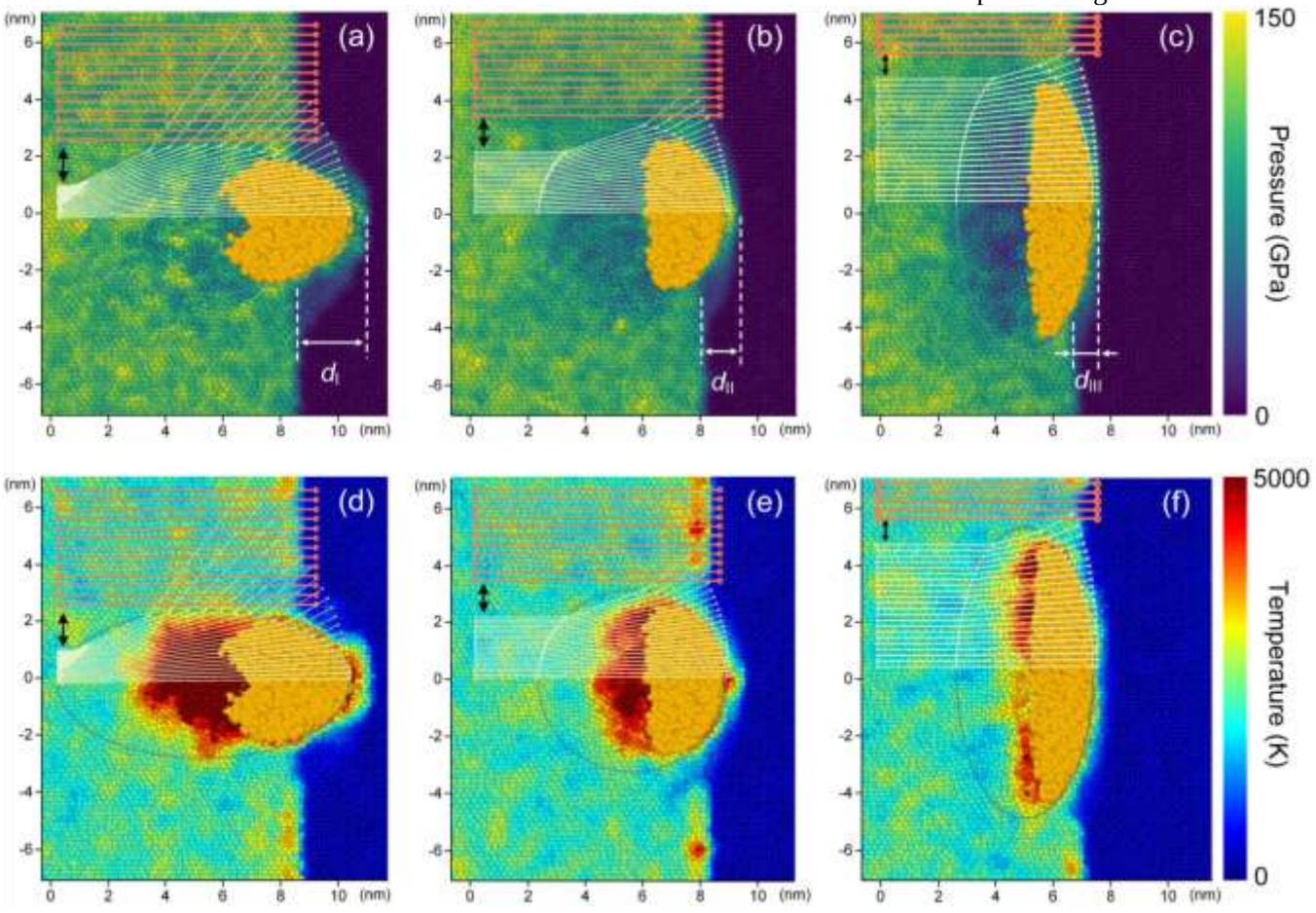

FIG. 9. The snapshots of (a) HB-I, (b) HB-II, and (c) HB-III colored by pressure and the snapshots of (d) HB-I, (e) HB-II, and (f) HB-III colored by temperature. The red line and the light green line, respectively, represent the shock wave trajectory that does not enter the He bubble and the shock wave trajectory that enters the He bubble obtained by theoretical analysis results. The areas marked by the black arrows indicate the total reflection regions.

theoretical analysis result is consistent with the simulation results. The wavefront broadening magnitude is quantified by the relative displacement d between the transmitted wavefront traversing the helium bubble and the undisturbed incident wavefront. There are significant differences in the wavefront broadening magnitude of the shock front for different types of He bubbles. The d_I, d_{II}, and d_{III} of HB-I, HB-II, and HB-III are equal to 3.0, 1.4, and 0.7 nm, respectively. The result shows that the shock front broadening extent follows the pattern $d_I > d_{II} > d_{III}$. It should be noted that $\theta_1 > \theta_2$. As θ_1 increases and approaches a critical value, θ_2 will reach 90° first. Once θ_1 exceeds this threshold, the shock wave cannot enter the helium bubble, but is completely reflected at the interface. The phenomenon is marked by the black arrows in Fig. 9. Since only the shock front is considered, He bubbles are assumed to remain in an uncompressed state when the shock wave passes through. The subsequent deformation of the He bubble does not affect the shape of the shock front. Therefore, the deformation of the He bubble can be neglected.

D. The surface failure induced by a He bubble

Vol. 13 No. 2 | Imp. Factor: 8.13
DOI: https://doi.org/10.5281/zenodo.15845920

To investigate the surface failure induced by different morphologies of He bubbles, we placed helium bubbles near the interface at a distance of 4 nm from the free surface and subjected them to a shock with a particle velocity of 2.0 km/s. The morphologies and sizes of He bubbles are consistent with the characteristics of He bubbles in the previous cases. Figure 10(a) shows the volume ratio of V/V_0 for the He bubble before rupture, where V is the volume of the He bubble and V_0 is the initial volume. The evolution of the near-surface He bubble undergoes three main stages as the same as the bulk He bubble: (I) compression, (II) relaxation, and (III) expansion. However, the near-surface He bubble also experiences another stage: (IV) rupture. During the compression stage, the bubble volume rapidly decreases. Subsequently, before the reflection of the shock wave from the free surface, the He bubble undergoes a brief relaxation stage. Finally, the He bubble expands until rupture occurs. The results indicate that HB-I has the

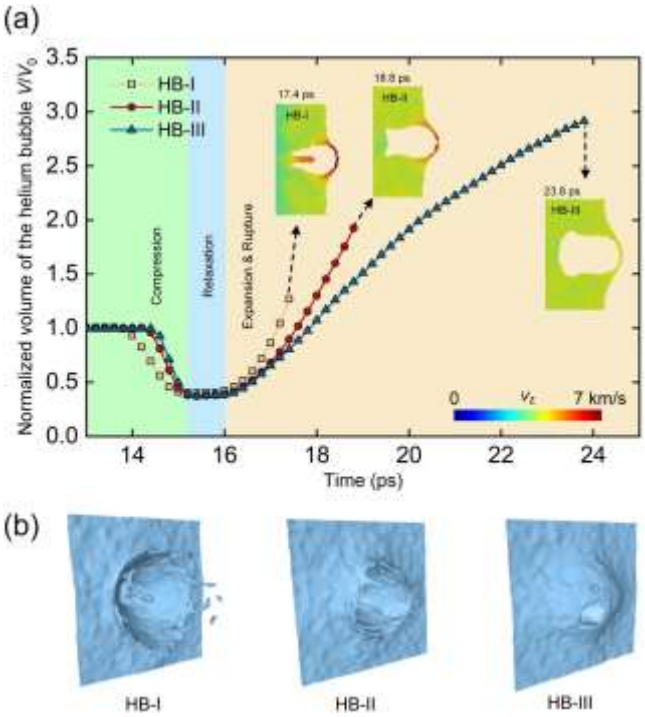

FIG. 10. (a) Temporal evolution of the volume ratio of the three types of He bubbles before rupture. The temporal evolution stages are distinguished by different background colors. The inset images show the microstructures of He bubbles at the rupture moment. The He atoms are removed for clarity. (b) Microstructure of the free surface after He bubble rupture.

fastest expansion rate after shock wave unloading, followed by HB-II, and HB-III exhibits the slowest expansion rate. Correspondingly, HB-I ruptures first, and HB-III ruptures latest under the same shock wave loading.

For HB-I, unlike the case of the bulk He bubble shown in Fig. 2(a), the internal jet generated by the compression of the He bubble did not disappear over time. Instead, after the He bubble ruptured at the free surface, the internal jet evolved into a surface jet. The rupture occurs the earliest for HB-I compared to the others. For HB-II, it also induced breakage of a free surface, but the severity of the breakage was less than that of HB-I. Furthermore, no internal jet was formed in HB-II under $u_p = 2.0$

Vol. 13 No. 2 | Imp. Factor: 8.13
DOI: https://doi.org/10.5281/zenodo.15845920

km/s. The rupture of HB-III occurs last, with the largest volume when rupture occurs than others. Figure 10(b) show the microstructures of the free surface after He bubble rupture, which is obtained by constructing a surface mesh method.[42] It indicates that the surface breakage induced by HB-III is the lightest among the three types of He bubbles.

As the shock intensity increases, the free surface will gradually transition to a failure state. There is a critical shock intensity at which surface failure occurs for three types of helium bubbles located 4 nm away from the free surface. The post-shock particle velocity thresholds corresponding to this critical intensity are

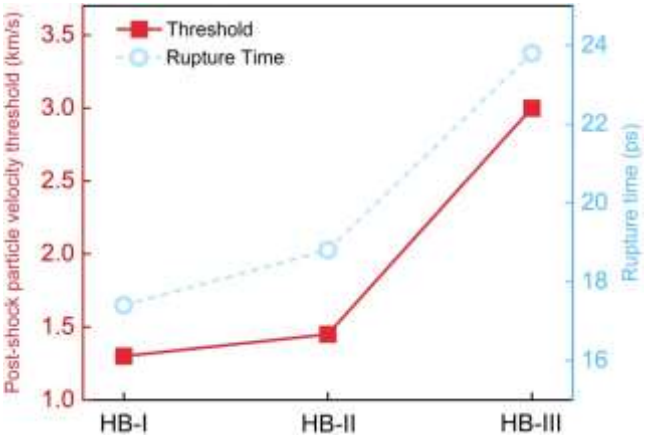

FIG. 11. The rupture times at u_p = 2.0 km/s for different types of He bubbles, as well as the post-shock particle velocity thresholds for rupture.

denoted as u_{dI}, u_{dII}, and u_{dIII} for HB-I, HB-II, and HB-III, respectively. As shown in Fig. 11, the post-shock particle velocity thresholds for surface failure induced by the helium bubble follow the trend $u_{dI} < u_{dII} < u_{dIII}$. The major axis of HB-III is oriented perpendicular to the shock direction, which reduces energy concentration and results in enhanced resistance to rupture under shock. Therefore, the critical velocity u_{dIII} is significantly higher than the others as shown in Fig. 11.

IV. CONCLUSIONS

We performed molecular dynamics simulations to investigate the evolution and thermodynamic response of nanoscale helium bubbles with different morphologies under shock wave loadings. The results show that the He bubble HB-I with the major axis aligned with the shock propagation direction induces the most severe temperature rise and the highest thermal energy accumulation in copper. It is attributed to its largest interface curvature, which generates a higher transverse velocity component perpendicular to the shock direction, thereby enhancing energy accumulation. HB-I also exhibits the most pronounced wavefront broadening effect, caused by the refraction of the incident shock wave at the helium–metal interface. In addition, the results indicate that the near-surface He bubble HB-I induced the most severe surface failure, as well as the fastest expansion rate and the earliest rupture time under the same shock loading. The post-shock particle velocity thresholds for surface failure induced by helium bubbles follow the trend of $u_{dI} < u_{dII} < u_{dIII}$.

ACKNOWLEDGMENTS

Financial supports for this work were provided by the National Key R&D Program of China (Grant No.

Vol. 13 No. 2 | Imp. Factor: 8.13
DOI: https://doi.org/10.5281/zenodo.15845920
2021YFB3802300), the National Key Laboratory of Shock Wave and Detonation Physics Fund (Grant No. 2023JCJQLB05401), and the National Natural Science Foundation of China (Grant Nos. 12202073 and 12302462).

AUTHOR DECLARATIONS

Conflict of Interest

The authors have no conflicts to disclose.

Author Contributions

Sheng-Ning Yan and Bao Wu contributed equally to this paper.

Sheng-Ning Yan: Conceptualization (equal); Investigation (equal); Methodology (equal); Writing – original draft (equal). Bao Wu: Funding acquisition (equal); Methodology (equal); Validation (equal); Writing – review & editing (equal). Xin-Xin Wang: Conceptualization (equal); Funding acquisition (equal); Writing – original draft (equal); Writing – review & editing (equal). Qiang Bao: Methodology (equal); Validation (equal). Hao-Nan Sui: Methodology (equal); Validation (equal). An-Min He: Validation (equal); Writing – review & editing (equal). Pei Wang: Conceptualization (equal); Funding acquisition (equal); Supervision (equal); Writing – review & editing (equal).

DATA AVAILABILITY

The data that support the findings of this study are available from the corresponding authors upon reasonable request.

REFERENCES

Bao, Q., Wu, B., Wang, X. X., Sui, H., Geng, H. Y., Shao, J. L., Sun, H. Q., He, M., & Wang, P. (2024). Helium bubble-induced thermal and mechanical effects in copper under shock: A molecular dynamics study. *Physics of Fluids, 36*(11), 112101. https://doi.org/10.1063/5.0185903

Bringa, M., Cazamias, J. U., Erhart, P., Stölken, J., Tanushev, N., Wirth, B. D., Rudd, R. E., & Caturla, M. J. (2004). Atomistic shock simulations of defect generation in metals. *Journal of Applied Physics, 96*(7), 3793–3799. https://doi.org/10.1063/1.1776631

Cherne, F. J., Hammerberg, J. E., Andrews, M. J., Karkhanis, V., & Ramaprabhu, P. (2015). Richtmyer–Meshkov mixing with complex initial conditions. *Journal of Applied Physics, 118*(18), 185901. https://doi.org/10.1063/1.4934927

Ding, M. S., Tian, L., Han, W. Z., Li, J., Ma, E., & Shan, Z. W. (2016). Nanoscale voids slow down dislocation climb in aluminum. *Physical Review Letters, 117*(21), 215501. https://doi.org/10.1103/PhysRevLett.117.215501

Fan, Q., Li, Q., Ding, J., Liang, Y., Shang, Z., Li, J., Su, R., Cho, J., Chen, D., Wang, Y., Wang, J., Wang, H., & Zhang, X. (2019). Mechanical behavior of helium-implanted tungsten: Bubble evolution and its interaction with dislocations. *Acta Materialia, 177*, 107–120. https://doi.org/10.1016/j.actamat.2019.07.028

Fensin, S., Jones, D., Martinez, D., Lear, C., & Payton, J. (2020). Investigating plasticity in copper through experimental methods. *Materials, 13*(6), 1270. https://doi.org/10.3390/ma13061270

Vol. 13 No. 2 | Imp. Factor: 8.13
DOI: https://doi.org/10.5281/zenodo.15845920

Glam, B., Eliezer, S., Moreno, D., Perelmutter, L., Sudai, M., & Eliezer, D. (2010). Dynamic fracture under high pressure: Experiments and models. *International Journal of Fracture, 163*(1), 217–224. https://doi.org/10.1007/s10704-009-9423-0

Glam, B., Moreno, D., Eliezer, S., & Eliezer, D. (2009). Interaction of helium bubbles with shock waves in copper. *Journal of Nuclear Materials, 393*(2), 230–234. https://doi.org/10.1016/j.jnucmat.2009.07.024

Glam, B., Strauss, M., Eliezer, S., & Moreno, D. (2014). Influence of helium nanobubbles on spallation in metals under dynamic loading. *International Journal of Impact Engineering, 65*, 1–12. https://doi.org/10.1016/j.ijimpeng.2013.10.008

Jiang, D. D., Shao, J. L., He, A. M., & Wang, P. (2023). Shock response of nanostructured copper containing helium bubbles. *Scripta Materialia, 234*, 115546. https://doi.org/10.1016/j.scriptamat.2023.115546

Jiang, D. D., Zhou, T. T., Wang, P., & He, A. M. (2022). Shock-induced damage and energy dissipation in nanobubble copper systems. *International Journal of Mechanical Sciences, 232*, 107585. https://doi.org/10.1016/j.ijmecsci.2022.107585

Katoh, Y., Ando, M., & Kohyama, A. (2003). Helium effects in fusion materials: Bubble growth and mechanical degradation. *Journal of Nuclear Materials, 323*(2), 251–262. https://doi.org/10.1016/j.jnucmat.2003.09.021

Kubota, A., Reisman, D. B., & Wolfer, W. G. (2006). Modeling shock response of helium-bubble copper. *Applied Physics Letters, 88*(24), 241924. https://doi.org/10.1063/1.2214120

Lear, R., Chancey, M. R., Flanagan, R. M., Gigax, J. G., Hoang, M. T., Jones, D. R., Kim, H., Martinez, D. T., Morrow, B. M., Mathew, N., Wang, Y., Li, N., Payton, J. R., Prime, M. B., & Fensin, S. J. (2023). Helium bubble evolution in irradiated copper alloys. *Acta Materialia, 254*, 118987. https://doi.org/10.1016/j.actamat.2023.118987

Li, Y., Chang, J., Zhang, L., & Song, P. (2021). Shock-induced effects in nanostructured copper with He bubbles. *Chinese Journal of High Pressure Physics, 35*(5), 58–63.

Li, B., Wang, L., E, J. C., Ma, H. H., & Luo, S. N. (2014). Shock wave interactions with nanoscale defects in metals. *Journal of Applied Physics, 116*(21), 213506. https://doi.org/10.1063/1.4902900

Mishin, Y., Mehl, M. J., Papaconstantopoulos, D. A., Voter, A. F., & Kress, J. D. (2001). Structural and elastic properties of copper: A tight-binding potential. *Physical Review B, 63*(22), 224106. https://doi.org/10.1103/PhysRevB.63.224106

Osetsky, Y. N., & Stoller, R. E. (2015). Void and bubble evolution in irradiated copper. *Journal of Nuclear Materials, 465*, 448–454. https://doi.org/10.1016/j.jnucmat.2015.06.038

Plimpton, S. (1995). Fast parallel algorithms for short-range molecular dynamics. *Journal of Computational Physics, 117*(1), 1–19. https://doi.org/10.1006/jcph.1995.1039

Vol. 13 No. 2 | Imp. Factor: 8.13
DOI: https://doi.org/10.5281/zenodo.15845920

Qi, M., He, H., Wang, Y., & Yan, S. (2007). Atomistic simulation of helium bubble effects in metals. *Chinese Journal of High Pressure Physics, 21*(2), 145–150.

Shao, J. L., Wang, P., He, A. M., Duan, S. Q., & Qin, C. S. (2014). A computational study of helium bubble stability in copper. *Modelling and Simulation in Materials Science and Engineering, 22*(2), 025012. https://doi.org/10.1088/0965-0393/22/2/025012

Schwartz, A. J., Wall, M. A., Zocco, T. G., & Wolfer, W. G. (2005). Microstructure of helium-bubble copper alloys after shock. *Philosophical Magazine, 85*(4–7), 479–488. https://doi.org/10.1080/14786430412331330184

Stukowski, A. (2014). Visualization and analysis of atomistic simulation data with OVITO. *JOM, 66*(3), 399–407. https://doi.org/10.1007/s11837-014-0882-0

Trinkaus, H., & Singh, B. N. (2003). Helium accumulation in metals: From atomic scale to continuum models. *Journal of Nuclear Materials, 323*(2), 229–242. https://doi.org/10.1016/j.jnucmat.2003.09.014

Ullmaier, H. (1997). Helium effects in metals under irradiation. *MRS Bulletin, 22*(4), 14–21. https://doi.org/10.1557/S0883769400032772

Wang, X. X., He, A. M., Yang, Y., Wang, P., & Wang, J. G. (2021). Simulation of dynamic failure in copper under shock compression. *Computational Materials Science, 188*, 110190. https://doi.org/10.1016/j.commatsci.2020.110190

Wang, X. X., Shao, J. L., Wu, B., Yan, S. N., He, A. M., & Wang, P. (2023). Shock-induced emission and wave evolution in nanobubble copper. *Physics of Fluids, 35*(5), 052112. https://doi.org/10.1063/5.0148997

Wang, Z. J., Allen, F. I., Shan, Z. W., & Hosemann, P. (2016). Evolution of helium bubbles and damage in metals under stress. *Acta Materialia, 121*, 78–84. https://doi.org/10.1016/j.actamat.2016.09.015

Wan, X., Yao, S., & Pei, X. (2022). Thermomechanical effects of helium nanobubbles in irradiated copper. *Chinese Journal of High Pressure Physics, 36*(1), 134–148.

Wu, H., Zhou, T., & Wang, P. (2022). Shock responses in He-bubble copper systems. *Journal of Nuclear Materials, 558*, 153404. https://doi.org/10.1016/j.jnucmat.2021.153404

Zhou, T. T., He, A. M., Wang, P., & Shao, J. L. (2019). Molecular dynamics study of helium nanobubbles in shocked copper. *Computational Materials Science, 162*, 255–267. https://doi.org/10.1016/j.commatsci.2019.02.006

Zhu, Q., Shao, J. L., & Wang, P. (2023). Modeling helium bubble evolution under dynamic loading. *Journal of Nuclear Materials, 574*, 154200. https://doi.org/10.1016/j.jnucmat.2023.154200

Zhu, Q., Shao, J. L., & Wang, P. (2023). Thermal responses in copper with helium nanobubbles. *Mechanics of Materials, 185*, 104755. https://doi.org/10.1016/j.mechmat.2023.104755